Conversion of Magnetic Energy to Plasma Kinetic Energy During Guide Field Magnetic Reconnection in the Laboratory

Sayak Bose[1,*] William Fox[1,2] Hantao Ji[1,2] Jongsoo Yoo[1] Aaron Goodman[3]
Andrew Alt[2] and Masaaki Yamada[1]

[1]*Princeton Plasma Physics Laboratory, Princeton, New Jersey 08540, USA*
[2]*Department of Astrophysical Sciences, Princeton University, New Jersey 08540, USA*
[3]*Department of Mechanical and Aerospace Engineering, Princeton University, New Jersey 08540, USA*

We present laboratory measurements showing the two-dimensional (2D) structure of energy conversion during magnetic reconnection with a guide field over the electron and ion diffusion regions, resolving the separate energy deposition on electrons and ions. We find that the electrons are energized by the parallel electric field at two locations, at the X line and around the separatrices. On the other hand, the ions are energized ballistically by the perpendicular electric field in the vicinity of the high-density separatrices. An energy balance calculation by evaluating the terms of the Poynting theorem shows that 40% of the magnetic energy is converted to particle energy, 2/3 of which is transferred to ions and 1/3 to electrons. Further analysis suggests that the energy deposited on particles manifests mostly in the form of thermal kinetic energy in the diffusion regions.

Magnetic reconnection is a fundamental process in plasmas that leads to a change in the magnetic field topology accompanied by the conversion of magnetic energy to plasma kinetic energy [1]. Often during reconnection, there is a component of the magnetic field called the guide field (GF) perpendicular to the plane of the antiparallel components. The GF reconnection is observed to energize electrons and ions in fusion plasmas [2,3], basic physics experiments [4–6], the solar wind [7], solar flares [8], and the Earth's magnetosphere [9–13].

Multiple mechanisms of electron [14–16] and ion energization [17,18] are proposed during GF reconnection. Satellite measurements of GF reconnection sites provide insight into kinetic-scale physics [9–13,19]. Sparse measurements by a few satellites, however, have not been sufficient to quantify particle energization on a global scale due to the complex structures around the reconnection site. Comprehensive laboratory measurements of key parameters under well-defined, repeatable conditions are ideal for complementing simulations and satellite observation. However, early GF reconnection experiments were only performed in a regime where ions were unmagnetized over the system size, and the ion skin depth was much larger than the system size [20].

In this Letter, we present the first laboratory measurements of two-dimensional (2D) profiles of energy deposition on electrons and ions during GF reconnection in the regime where ions were sufficiently magnetized over the system size, and the ion skin depth was small enough for the electron and ion dynamics to be coupled. We significantly extend prior GF reconnection experiments [21,22]

by obtaining separate measurements of electron and ion flows, allowing determination of energy deposition onto each species. The energy deposition onto electrons is dominated by $\mathbf{E}_\parallel$, in two regions of the reconnection layer: around the X line and near the separatrices. The energy deposition on ions is dominated by $\mathbf{E}_\perp$ which is sufficiently strong to demagnetize and ballistically energize ions, in the vicinity of the high-density separatrices where electrons flow against the electric field. Furthermore, we determine how the energy is partitioned during GF reconnection, including enhancement of electron and ion kinetic energy in the form of thermal energy.

The experiments were conducted in the Magnetic Reconnection eXperiment (MRX) [23,24] (see Appendix for methodology) for a moderate GF of magnitude 122 G at the X line. The upstream reconnecting magnetic field at a distance of $1\rho_s$ from the X line is around 131 G, where $\rho_s = 3.9$ cm is the ion sound gyroradius calculated using electron temperature (T_e) and the total upstream magnetic field. A typical reconnection electric field ranges from 1 to 1.5 V/cm. The classical Spitzer resistivity accounts for approximately 9% of the reconnection electric field.

The features of the reconnection layer are shown in Fig. 1. Figure 1(a) displays representative magnetic field lines in the reconnection plane, i.e., the r-z plane. The 2D profile of the out-of-plane magnetic field (B_y) in Fig. 1(b) exhibits a quadrupolar structure, indicating the presence of two-fluid effects [25]. The plasma potential calculated using $V_p = V_f + 3.7T_e$ [26] also displays a quadrupolar structure [see Fig. 1(c)] [27]. Here V_p and V_f are the plasma
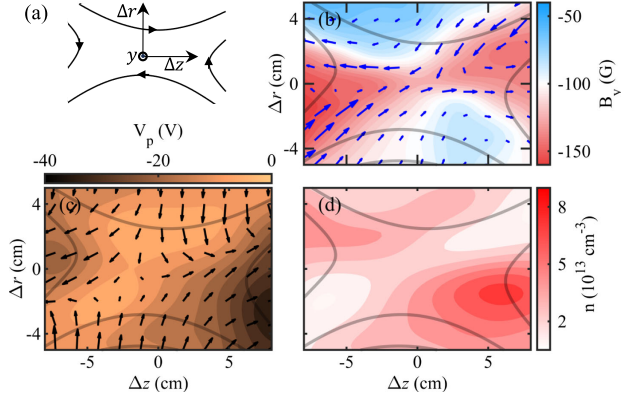
FIG. 1. (a) Representative reconnecting and reconnected magnetic field lines, and the coordinate system with respect to the X point. The 2D profiles of the (b) out of plane magnetic field, (c) plasma potential, and (d) density in the reconnection plane. The blue arrows in (b) represent the electron velocity vectors, while the black arrows in (c) represent the ion velocity vectors.

potential and floating potential, respectively. The 2D profile of density (n) reveals a pair of high density and low density regions in the vicinity of the separatrices [Fig. 1(d)] [22]. The n and V_p data exhibits a correlation; n is high at regions where V_p is more negative.

The arrows in Fig. 1(b) depict the flow of electrons in the reconnection region. The electron velocity is derived from the current profile using $\mathbf{v}_e = \mathbf{v}_i - \mathbf{J}/en$, where e is the quantum of electric charge, $\mathbf{J}$ is the surface current density, and $\mathbf{v}_e$ and $\mathbf{v}_i$ are the electron and ion velocity, respectively. The electron velocity vectors show that electrons enter the reconnection layer along a pair of low density separatrices and are ejected out through the high density side of the reconnection layer. The electron inflow velocity is greater than the outflow velocity. The ion flow velocity vectors in the reconnection plane are shown in Fig. 1(c). A comparison of the electron and ion velocity vectors unambiguously demonstrates that the trajectories of the electron and ion fluids are significantly different in the reconnection layer.

The conversion of the magnetic energy to the plasma kinetic energy is mediated by an electric field which is given by Ohm's law (the electron momentum equation),

$$\mathbf{E} + \mathbf{v}_e \times \mathbf{B} = -\frac{m_e}{e}\frac{d\mathbf{v}_e}{dt} - \frac{\nabla \cdot \overleftrightarrow{P}_e}{en} + \eta_\parallel \mathbf{J}_\parallel + \eta_\perp \mathbf{J}_\perp, \quad (1)$$

where m_e is the mass of the electron, $\overleftrightarrow{P}_e$ is the electron pressure tensor, and η is the Spitzer resistivity. The power deposition per unit volume on particles due to the nonideal terms of Ohm's law on the rhs of Eq. (1) is given by $D_e = \mathbf{J} \cdot \mathbf{E}'$, where $\mathbf{E}' = \mathbf{E} + \mathbf{v}_e \times \mathbf{B}$, the electric field due to nonideal terms [28]. A positive value of D_e indicates the region of magnetic energy deposition where the frozen-in condition of the electrons is violated, i.e.,

$\mathbf{E}' = \mathbf{E} + \mathbf{v}_e \times \mathbf{B} \neq 0$. However, D_e does not differentiate between energy deposition onto electrons and ions. While the electrons can only be energized by the nonideal terms because $\mathbf{v}_e \cdot (\mathbf{v}_e \times \mathbf{B}) = 0$, the ions may gain energy from the nonideal terms as well as from the $-(\mathbf{v}_e \times \mathbf{B})$ term. Therefore, to quantify the rate of work done on electrons and ions we calculate $W_e = \mathbf{J}_e \cdot \mathbf{E} (= \mathbf{J}_e \cdot \mathbf{E}')$ and $W_i = \mathbf{J}_i \cdot \mathbf{E}$, respectively.

The 2D profile of D_e depicted in Fig. 2(a) shows that the energy conversion from the magnetic field to the plasma kinetic energy is mediated by $\mathbf{E}'$ at multiple locations in the reconnection plane. The rate of energy deposition per unit volume is most intense near the X line where D_e is as high as 80 W/cm³. D_e is also positive in the electron inflow region near the separatrices revealing regions of particle energization away from the X line. However, in the region with a strong electron outflow, the electrons flow against $\mathbf{E}'$. The representative 1-σ error bars are shown in Fig. 2(e) which depicts a 1D cut of D_e across the X line.

A comparison of the 2D profiles of D_e [Fig. 2(a)], W_e [Fig. 2(b)], and W_i [Fig. 2(f)] shows a remarkable similarity between D_e and W_e. This resemblance suggests that the nonideal terms of Ohm's law channel most of the magnetic energy to electrons.

Since the dynamics of charged particles parallel and perpendicular to the magnetic field are different, it is instructive to calculate the energy deposition driven by $\mathbf{E}_\parallel$ and $\mathbf{E}_\perp$. $W_{e,\parallel}$, $W_{e,\perp}$, $W_{i,\parallel}$, and $W_{i,\perp}$ are depicted in Figs. 2(c), 2(d), 2(g), and 2(h), respectively. $W_{e,\parallel}$ is computed using $J_{e,\parallel} = \mathbf{J}_e \cdot \hat{\mathbf{b}}$ and $E_\parallel = \mathbf{E} \cdot \hat{\mathbf{b}}$, where $\hat{\mathbf{b}}$ is a unit vector along the magnetic field. $W_{e,\perp}$ is determined from the dot product of $\mathbf{J}_{e,\perp} = \mathbf{J}_e - \mathbf{J}_{e,\parallel}$ and $\mathbf{E}_\perp = \mathbf{E} - \mathbf{E}_\parallel$. Similarly, we have worked out $W_{i,\parallel}$ and $W_{i,\perp}$.

The electrons are energized by $E_\parallel$ in two regions of the reconnection layer: most intensely near the X line and additionally in the vicinity of the separatrices over the ion scale, as shown in Fig. 2(c). Previously, Fox et al. [22] have shown that $\mathbf{E}_\parallel$ in the ion diffusion region is approximately supported by the pressure gradient term of Ohm's law, i.e., $\mathbf{E}_\parallel \approx -\nabla_\parallel P_e/en$. Extending on that finding, we observe $J_{e,\parallel}E_\parallel \approx \mathbf{v}_{e,\parallel} \cdot \nabla_\parallel P_e$. For example, at $\Delta r = -2.25$ cm and $\Delta z = 5.75$ cm, $J_{e,\parallel}E_\parallel$ and $\mathbf{v}_{e,\parallel} \cdot \nabla_\parallel P_e$ are 31 W/cm³ and 27 W/cm³, respectively. The positive and negative values of $J_{e,\parallel}E_\parallel$ in the ion diffusion region indicate compression and decompression of the electron fluid. Similarly, the negative values of $\mathbf{J}_{e,\perp} \cdot \mathbf{E}_\perp$ in the electron outflow region in Fig. 2(d) suggest decompression.

The structure of $W_{e,\parallel}$ in Fig. 2(c) is rather interesting. The electrons approaching the reconnection layer along $\mathbf{B}$ are continuously under the influence of $\mathbf{E}_\parallel$ until the X line. In natural systems, where the electron mean free path is significantly large compared to laboratory experiments, an "acceleration-channel"-like feature where electrons are continuously under the influence of the driver term, $\mathbf{E}_\parallel$,
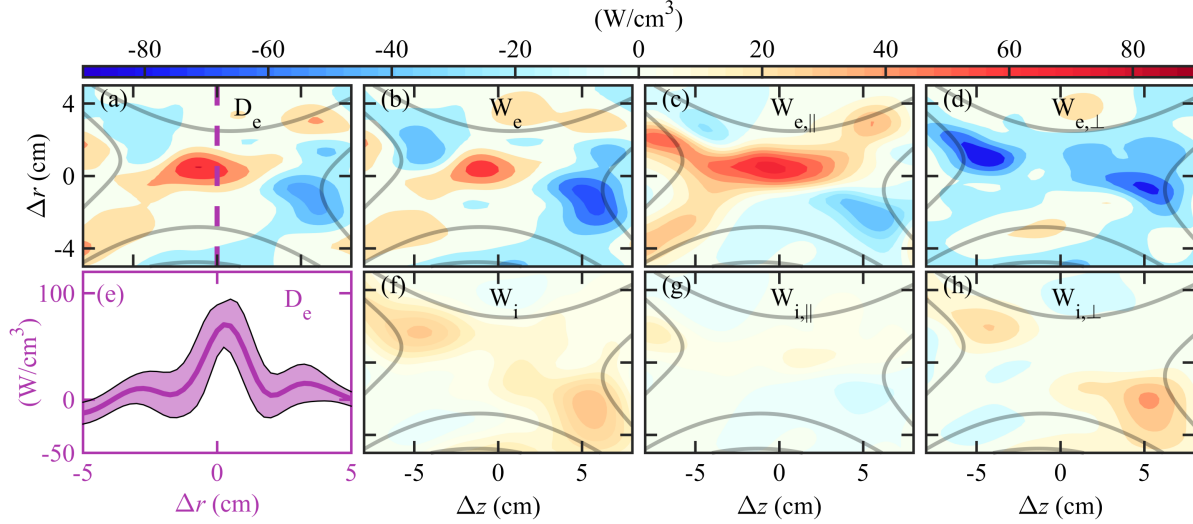
FIG. 2. 2D profiles of scalar products that quantify power deposition on electrons and ions. (a) $D_e = \mathbf{J} \cdot \mathbf{E}'$, (b) $W_e = \mathbf{J}_e \cdot \mathbf{E}$, (c) $W_{e,\parallel} = J_{e,\parallel} E_\parallel$, (d) $W_{e,\perp} = \mathbf{J}_{e,\perp} \cdot \mathbf{E}_\perp$, (f) $W_i = \mathbf{J}_i \cdot \mathbf{E}$, (g) $W_{i,\parallel} = J_{i,\parallel} E_\parallel$, and (h) $W_{i,\perp} = \mathbf{J}_{i,\perp} \cdot \mathbf{E}_\perp$. The remaining plot in (e) is a 1D cut of D_e to illustrate the representative 1-σ error bars.

over large distances may explain the observation of high energy electrons associated with GF reconnection [29,30].

The 2D profile of W_i depicted in Fig. 2(f) shows that the regions of intense ion energization are well-structured and located in the electron outflow region, and are dominated by $\mathbf{E}_\perp$ [Fig. 2(h)] over $E_\parallel$ [Fig. 2(g)]. $E_\perp$ varies from 3 to 6 V/cm in the region of intense energization. Interestingly, the 2D profiles of W_e [Fig. 2(b)] and W_i [Fig. 2(f)] show that the regions of electron and ion energization are rather complementary. The electrons are energized near the low-density separatrices and at the X line, while the ions gain energy in the vicinity of the high-density separatrices where the electrons work against the electric field. This suggest that electrons may transfer their energy to ions via the electric field.

$\mathbf{E}_\perp$ can energize the ions in two ways: the ions can be energized ballistically when ions are unmagnetized, or $\mathbf{E}_\perp$ can drive ion polarization drift that adiabatically increases the ion velocity to reach the $\mathbf{E} \times \mathbf{B}$ outflow velocity. To distinguish between these two processes we compare the relevant length and time scales with the estimated ion gyroradius (ρ_i) and gyroperiod (τ_i), respectively. The length scale of the magnetic field $L_B = |B/\nabla B|$ in the region of ion energization at $\Delta z = -5$ cm and $\Delta r = 1$ cm is 6 cm which is comparable to $\rho_i = 4$ cm. We used $T_i = 6.5$ eV measured by ion Doppler spectroscopy and the local value of B to estimate ρ_i. The width of the ion energization region in both the upper left and lower right of Fig. 2(f) is ≈ 5 cm, which is comparable to ρ_i. The ion transit time, τ, through the region of intense ion energization in the upper left of Fig. 2(f) is ≈ 7 μs, which is almost a third of $\tau_i \approx 20$ μs. Similarly in the lower right $\tau < \tau_i$. Thus, we conclude that strong $\mathbf{E}_\perp$ energize the demagnetized ions ballistically.

The energy partition among electrons, ions, and other channels during GF reconnection is analyzed by calculating the terms of the Poynting theorem,

$$-\int \frac{\partial}{\partial t}\left(\frac{B^2}{2\mu_0}\right) d^3x = \int \nabla \cdot (\mathbf{S_{in}} + \mathbf{S_{rec}} + \mathbf{S_o}) d^3x$$
$$+ \int (\mathbf{J}_e \cdot \mathbf{E} + \mathbf{J}_i \cdot \mathbf{E}) d^3x, \qquad (2)$$

where integration is carried out over reconnection volume assuming toroidal symmetry. Here, $\mathbf{S_{in}} = (E_y B_z/\mu_0)\hat{\mathbf{r}}$ is the incoming Poynting flux associated with the reconnecting magnetic field and the reconnection electric field, and the outgoing Poynting flux is divided into $\mathbf{S_{rec}}$ and $\mathbf{S_o}$. The $\mathbf{S_{rec}} = -(E_y B_r/\mu_0)\hat{\mathbf{z}}$ is associated with the reconnected magnetic field and the reconnection electric field. While $\mathbf{S_o} = (E_r B_y/\mu_0)\hat{\mathbf{z}} - (E_z B_y/\mu_0)\hat{\mathbf{r}}$, is associated with the Hall magnetic field superimposed on the guide field, and the electrostatic electric fields.

The results of the Poynting theorem analysis are shown in Fig. 3. The reconnecting magnetic field delivers 1.54 MW of power to the reconnection layer. There is a slight decrease of magnetic field during reconnection resulting in a reduction of 0.15 MW in magnetic power. 1 MW of magnetic power flows out of the reconnection layer. The bulk of the outflow is due to the Poynting vector associated with the reconnected magnetic field, which is 0.63 MW, while the rest is accounted for by the outgoing toroidal magnetic field. Around 40% of the magnetic energy is deposited on the particles, 1/3 of which goes to electrons and 2/3 to ions.

The energy deposited on electrons and ions may manifest in the form of thermal energy, causing an increase in temperature, or causing acceleration resulting in a gain of
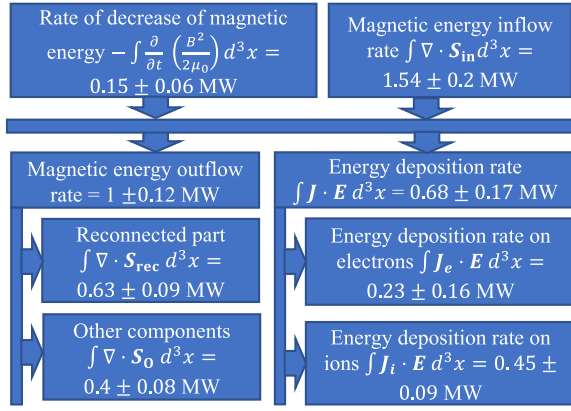
Rate of decrease of magnetic energy $-\int \frac{\partial}{\partial t}\left(\frac{B^2}{2\mu_0}\right)d^3x =$ 0.15 ± 0.06 MW	Magnetic energy inflow rate $\int \nabla \cdot S_{in} d^3x =$ 1.54 ± 0.2 MW
Magnetic energy outflow rate = 1 ±0.12 MW	Energy deposition rate $\int J \cdot E\, d^3x = 0.68 \pm 0.17$ MW
Reconnected part $\int \nabla \cdot S_{rec}\, d^3x =$ 0.63 ± 0.09 MW	Energy deposition rate on electrons $\int J_e \cdot E\, d^3x =$ 0.23 ± 0.16 MW
Other components $\int \nabla \cdot S_0\, d^3x =$ 0.4 ± 0.08 MW	Energy deposition rate on ions $\int J_i \cdot E\, d^3x = 0.45 \pm$ 0.09 MW

FIG. 3. Energy partition during GF reconnection during quasisteady period. The time variations of the energy partition quantities are within the error bars. The integration box covers an area of $4.1 \times 4.4 \rho_s$.

flow energy. The electron temperature measurement showed an enhancement in T_e in the vicinity of the X line where a significant amount of energy is deposited on electrons [see Fig. 2(b) for $J_e \cdot E$]. Figure 4 shows the radial variation of T_e. We observe that T_e increases from 5 eV at 5 cm away from the X line to 8 eV at the X line taken at $\Delta z = 0$. This increase in T_e is more than 50% and beyond the measurement uncertainty. The change in the electron thermal energy per unit time estimated using $\Delta W_{H,e} \approx \int \nabla \cdot (\frac{5}{2} n T_e v_e) d^3x$ is ~ 0.1 MW. This is smaller but on the same order as the magnetic energy deposition rate on electrons calculated by $\int J_e \cdot E\, d^3x$. The change in the electron flow energy per unit time is negligibly small $[\Delta W_{flow,e} \approx \int \nabla \cdot (\frac{1}{2} m_e n v_e^2 v_e) d^3x < 7$ W$]$ because of the low mass of electrons. Therefore, the rate of energy deposited on electrons not observed in $\Delta W_{H,e}$ is expected to be accounted for by loss mechanisms like the thermal conductivity parallel to the magnetic field [31–34]. This is expected to be large as it scales as $T_e^{7/2}$ but is difficult to estimate due to its sensitivity to the T_e gradient.

The T_i measurements suggest an increase in ion thermal energy during GF reconnection. In the right half of the reconnection plane near the exhaust, T_i is 9 eV, while in the left half exhaust T_i is 6.5 eV. T_i could not be measured in the upstream region due to low emission (due to low T_e)
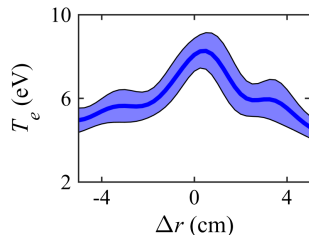

FIG. 4. Radial variation of T_e at $\Delta z = 0$ cm.

there. Nevertheless, previous MRX experiments [31] have shown that $T_i \approx T_e$ in the upstream region. Using this assumption, we estimate the increase in the thermal energy of the ions per unit time to be ~ 0.2 MW. This is within a factor of 2–3 of $\int J_i \cdot E\, d^3x$. However, the change in the ion flow energy per unit time is negligibly small $[\Delta W_{flow,i} \approx \int \nabla \cdot (\frac{1}{2} m_i n v_i^2 v_i) d^3x < 0.02$ MW$]$ as the ion flow measurements are confined to the ion diffusion region limiting the formation of an Alfvénic outflow.

The gap between $\int J_i \cdot E\, d^3x$ and the increase in ion thermal energy per unit time is expected to be accounted for by loss channels. A well-known energy loss mechanism for ions in MRX is the charge exchange collision with neutrals [33]. The measured neutral temperature of 3.3 eV during GF reconnection in the downstream region supports ion energy loss via the charge exchange mechanism. Assuming a uniform neutral density in the reconnection layer we estimate that the maximum ion energy loss per unit time to neutrals to be ~ 0.15 MW. In addition, ion energy loss is also expected to occur due to thermal conduction to the exhaust [31].

The above analysis showed that similar energy partition occur between electrons and ions during GF reconnection as in antiparallel reconnection [32]. This is interesting as there are significant differences between GF and antiparallel reconnection beyond the obvious presence of GF. The 2D profile of V_p and n exhibits a tilted quadrupolar structure in GF reconnection which is different from antiparallel reconnection. The electrons are energized by $E_\parallel$ and the electron inflow velocity is greater than the outflow velocity in GF reconnection, while in the antiparallel case, $E_\perp$ energizes the electrons, and the electron outflow velocity is greater than the inflow velocity [32,33]. The regions of ion energization are structured in GF reconnection. The ions gain energy in the vicinity of high density separatrices with spatial extent of around ρ_i, in contrast to during the antiparallel reconnection where the ions gain energy over a wide region in the exhaust [35]. Our experiment provides noteworthy constraints by identifying factors that may not appreciably affect the energy partition between the electrons and ions in the reconnection layer.

In summary, to study the conversion of the magnetic energy to the plasma kinetic energy during GF reconnection, we have compared 2D profiles of key energy deposition scalar products, $J \cdot E'$, $J_e \cdot E$, $J_{e,\parallel} E_\parallel$, $J_{e,\perp} \cdot E_\perp$, $J_i \cdot E$, $J_{i,\parallel} E_\parallel$, and $J_{i,\perp} \cdot E_\perp$. The electrons entering the reconnection layer along B are energized by $E_\parallel$ in the vicinity of the low-density separatrices. $E_\parallel$ energizes electrons all the way until the X line forming an acceleration-channel-like feature. The electron energization is most intense at the X line. The outgoing electrons work against the electric field near the high density separatrices. The ions are energized ballistically by $E_\perp$ in the vicinity of the high density separatrices in the outflow region. The energy conversion results are complemented by 2D

measurements of physical quantities that characterize the reconnection layer and provide references to compare our results to relevant regions in space observations, other laboratory experiments, and simulations.

The energy balance analysis by evaluating the terms of the Poynting theorem shows that 40% of the magnetic energy is deposited on particles with a $1:2$ ratio to electrons and ions. Additional measurements showed that the energy deposited on electrons manifests as thermal energy, part of which increases T_e while the rest is most probably transported to the exhaust by heat conduction. The energy deposited on ions enhances T_i with a dominant loss due to charge exchange collisions and also loss due to thermal conduction is expected. Future work would be to experimentally evaluate important terms of the electron and ion energy transport equations [33,36] so that their temperature increases can be understood in the context of finite energy transport and loss channels in the reconnection layer.

Data underlying the results presented in this Letter will be made available via Princeton University's data repository upon publication.

Appendix: Methodology.—The experiments are conducted in the Magnetic Reconnection eXperiment (MRX) [23,24]. A schematic of the experiment is shown in Fig. 5. The flux cores house the toroidal field (TF) and the poloidal field (PF) coils. The PF coils are used to produce antiparallel magnetic fields in the poloidal (r-z) plane of MRX. The toroidal GF, $-B_y\hat{y}$, is produced by passing a current through an axial conductor. A time-varying current
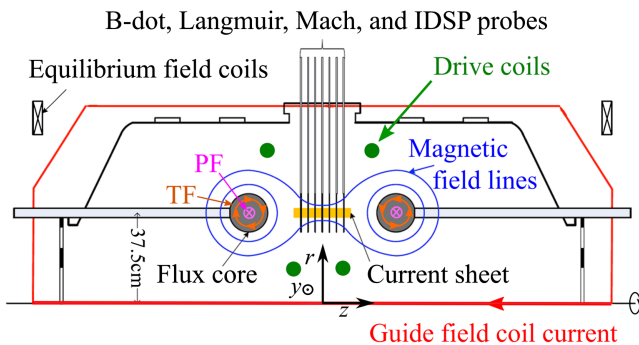

FIG. 5. Schematic of MRX showing the adopted coordinate system (r, y, z), the coils used to induce and drive reconnection, and different diagnostics used for making measurements. See the text and Refs. [22–24] for detailed description.

through the TF coils produces an inductive electric field that breaks down the gas to produce plasma. Reconnection is driven by inducing the radial inflow and axial outflow of the plasma from the reconnection layer by increasing the current in the upstream drive coils and ramping down the current in the PF coils. The reconnection is quasisteady in this mode of operation where the time scale of variation of the plasma current is greater than the ion-transit time. The data reported in this Letter were acquired during the quasisteady period as in previous experiments on MRX [21,22,31–33,35].

The experiments are carried out using Helium gas with a fill pressure of 4×10^{-3} Torr. Multiple triaxial B-dot probe arrays covering the reconnection layer are used for the magnetic-field measurements. The current density is calculated from the magnetic field using Ampère's law, $\mathbf{J} = \nabla \times \mathbf{B}/\mu_0$, where μ_0 is the permeability of free space. The inductive reconnection electric field, E_y, is determined from the rate of change of poloidal magnetic flux using Faraday's law assuming toroidal symmetry.

The electron density (n), temperature (T_e), and floating potential (V_f) are measured using a Langmuir probe [34]. The ion velocity, $\mathbf{v}_i$, is measured using Mach probes, which were calibrated using the ion velocity measured by the ion Doppler spectroscopy probe [34,35]. The electric probes are scanned between shots to sample the r-z plane. A total of 1,700 shots are scrutinized to assemble a refined dataset, based on consistency in magnetic-field structure and reference Langmuir probe data. A minor shot-to-shot variation in the X-line location is corrected by using the relative position of the probes with respect to the X line.

Gaussian process regression (GPR) [37], a class of machine learning algorithms, is utilized to construct 2D data planes from the discrete datasets of electric probes. GPR makes predictions using the trends in the dataset without assuming any specific functional form. We train a GPR model with a radial basis function kernel for each directly measured quantity using the discrete dataset [38]. The mean profiles and variances are extracted from the posterior of the trained GPR model. The error propagation analysis for composite quantities (for example, $\mathbf{J}_i = en\mathbf{v}_i$) is done using a Monte Carlo method. Samples are drawn randomly from the profiles of input quantities (n and $\mathbf{v}_i$) according to their respective uncertainty estimates. These samples are used to construct an ensemble of possible realizations of outputs (a set of $\mathbf{J}_i$) from which variances are calculated [39]. Refer to the Supplemental Material [40] for more details on the application of GPR, and error analysis.

*sbose@princeton.edu

[1] D. Biskamp, *Magnetic Reconnection in Plasmas*, Cambridge Monographs on Plasma Physics (Cambridge University Press, Cambridge, England, 2000).

[2] Y. Ono, H. Tanabe, T. Yamada, K. Gi, T. Watanabe, T. Ii, M. Gryaznevich, R. Scannell, N. Conway, B. Crowley *et al.*, Phys. Plasmas **22**, 055708 (2015).

[3] H. Tanabe, T. Yamada, T. Watanabe, K. Gi, M. Inomoto, R. Imazawa, M. Gryaznevich, R. Scannell, N. Conway, C. Michael *et al.*, Nucl. Fusion **57**, 056037 (2017).

[4] A. Stark, W. Fox, J. Egedal, O. Grulke, and T. Klinger, Phys. Rev. Lett. **95**, 235005 (2005).

[5] R. Stenzel, W. Gekelman, and N. Wild, J. Geophys. Res. **87**, 111 (1982).

[6] T. D. Tharp, M. Yamada, H. Ji, E. Lawrence, S. Dorfman, C. E. Myers, and J. Yoo, Phys. Rev. Lett. **109**, 165002 (2012).

[7] T. Phan, S. Bale, J. Eastwood, B. Lavraud, J. Drake, M. Oieroset, M. Shay, M. Pulupa, M. Stevens, R. MacDowall *et al.*, Astrophys. J. Suppl. Ser. **246**, 34 (2020).

[8] B. Chen, C. Shen, D. E. Gary, K. K. Reeves, G. D. Fleishman, S. Yu, F. Guo, S. Krucker, J. Lin, G. M. Nita *et al.*, Nat. Astron. **4**, 1140 (2020).

[9] R. E. Ergun, K. A. Goodrich, F. D. Wilder, J. C. Holmes, J. E. Stawarz, S. Eriksson, A. P. Sturner, D. M. Malaspina, M. E. Usanova, R. B. Torbert *et al.*, Phys. Rev. Lett. **116**, 235102 (2016).

[10] M. Øieroset, T. Phan, C. Haggerty, M. A. Shay, J. P. Eastwood, D. J. Gershman, J. F. Drake, M. Fujimoto, R. Ergun, F. Mozer *et al.*, Geophys. Res. Lett. **43**, 5536 (2016).

[11] F. D. Wilder, R. E. Ergun, S. Eriksson, T. D. Phan, J. L. Burch, N. Ahmadi, K. A. Goodrich, D. L. Newman, K. L. Trattner, R. B. Torbert *et al.*, Phys. Rev. Lett. **118**, 265101 (2017).

[12] Z. Li and M. Zhang, Astrophys. J. **888**, 5 (2019).

[13] S. Eriksson, F. D. Wilder, R. E. Ergun, S. J. Schwartz, P. A. Cassak, J. L. Burch, L.-J. Chen, R. B. Torbert, T. D. Phan, B. Lavraud *et al.*, Phys. Rev. Lett. **117**, 015001 (2016).

[14] F. Pucci, S. Usami, H. Ji, X. Guo, R. Horiuchi, S. Okamura, W. Fox, J. Jara-Almonte, M. Yamada, and J. Yoo, Phys. Plasmas **25**, 122111 (2018).

[15] X. Guo, R. Horiuchi, C. Cheng, Y. Kaminou, and Y. Ono, Phys. Plasmas **24**, 032901 (2017).

[16] C. Huang, Q. Lu, and S. Wang, Phys. Plasmas **17**, 072306 (2010).

[17] R. G. Kleva, J. Drake, and F. Waelbroeck, Phys. Plasmas **2**, 23 (1995).

[18] K. Knizhnik, M. Swisdak, and J. F. Drake, Astrophys. J. Lett. **743**, L35 (2011).

[19] K. Genestreti, J. Burch, P. Cassak, R. Torbert, R. Ergun, A. Varsani, T. Phan, B. Giles, C. Russell, S. Wang *et al.*, J. Geophys. Res. **122**, 11 (2017).

[20] N. Wild, W. Gekelman, and R. L. Stenzel, Phys. Rev. Lett. **46**, 339 (1981).

[21] W. Fox, F. D. Wilder, S. Eriksson, J. Jara-Almonte, F. Pucci, J. Yoo, H. Ji, M. Yamada, R. Ergun, M. Oieroset *et al.*, Geophys. Res. Lett. **45**, 12 (2018).

[22] W. Fox, F. Sciortino, A. V. Stechow, J. Jara-Almonte, J. Yoo, H. Ji, and M. Yamada, Phys. Rev. Lett. **118**, 125002 (2017).

[23] M. Yamada, H. Ji, S. Hsu, T. Carter, R. Kulsrud, N. Bretz, F. Jobes, Y. Ono, and F. Perkins, Phys. Plasmas **4**, 1936 (1997).

[24] H. Ji, Y. Ren, M. Yamada, S. Dorfman, W. Daughton, and S. Gerhardt, Geophys. Res. Lett. **35** (2008).

[25] D. A. Uzdensky and R. M. Kulsrud, Phys. Plasmas **13**, 062305 (2006).

[26] H. Ji, H. Toyama, K. Yamagishi, S. Shinohara, A. Fujisawa, and K. Miyamoto, Rev. Sci. Instrum. **62**, 2326 (1991).

[27] J. Egedal, A. Fasoli, and J. Nazemi, Phys. Rev. Lett. **90**, 135003 (2003).

[28] S. Zenitani, M. Hesse, A. Klimas, and M. Kuznetsova, Phys. Rev. Lett. **106**, 195003 (2011).

[29] G. D. Holman, Adv. Space Res. **35**, 1669 (2005).

[30] A. Abdo, M. Ackermann, M. Ajello, A. Allafort, L. Baldini, J. Ballet, G. Barbiellini, D. Bastieri, K. Bechtol, R. Bellazzini *et al.*, Science **331**, 739 (2011).

[31] J. Yoo, M. Yamada, H. Ji, J. Jara-Almonte, and C. E. Myers, Phys. Plasmas **21**, 055706 (2014).

[32] M. Yamada, J. Yoo, J. Jara-Almonte, H. Ji, R. M. Kulsrud, and C. E. Myers, Nat. Commun. **5**, 1 (2014).

[33] M. Yamada, J. Yoo, J. Jara-Almonte, W. Daughton, H. Ji, R. M. Kulsrud, and C. E. Myers, Phys. Plasmas **22**, 056501 (2015).

[34] J. Yoo, Experimental studies of particle acceleration and heating during magnetic reconnection, Ph.D. thesis, Princeton University (2013).

[35] J. Yoo, M. Yamada, H. Ji, and C. E. Myers, Phys. Rev. Lett. **110**, 215007 (2013).

[36] S. I. Braginskii, Rev. Plasma Phys. **1**, 205 (1965).

[37] C. E. Rasmussen, *Gaussian Processes for Machine Learning*, Adaptive Computation and Machine Learning Series (MIT Press, Cambridge, MA, 2005).

[38] F. Pedregosa, G. Varoquaux, A. Gramfort, V. Michel, B. Thirion, O. Grisel, M. Blondel, P. Prettenhofer, R. Weiss, V. Dubourg, J. Vanderplas, A. Passos, D. Cournapeau, M. Brucher, M. Perrot, and E. Duchesnay, J. Mach. Learn. Res. **12**, 2825 (2011).

[39] M. Chilenski, M. Greenwald, Y. Marzouk, N. Howard, A. White, J. Rice, and J. Walk, Nucl. Fusion **55**, 023012 (2015).

[40] See Supplemental Material at http://link.aps.org/supplemental/10.1103/PhysRevLett.132.205102 for more information on the application of Gaussian process regression for reconstruction of 2D data planes from discrete measurements, and error propagation. The Supplemental Material also includes Refs. [41–45].

[41] A. Mathews and J. W. Hughes, IEEE Trans. Plasma Sci. **49**, 3841 (2021).

[42] J. Wang, Comput. Sci. Eng. **25**, C4 (2023).

[43] Q.-H. Zhang and Y.-Q. Ni, IEEE Trans. Signal Process. **68**, 3450 (2020).

[44] M. Chilenski, M. Greenwald, A. Hubbard, J. Hughes, J. Lee, Y. Marzouk, J. Rice, and A. White, Nucl. Fusion **57**, 126013 (2017).

[45] Gaussian processes, https://scikit-learn.org/stable/modules/gaussian_process.html, (Online; accessed 5-July-2023).